bioRxiv preprint doi: https://doi.org/10.1101/2022.11.28.517870; this version posted November 29, 2022. The copyright holder for this preprint (which was not certified by peer review) is the author/funder. All rights reserved. No reuse allowed without permission.

The human sperm head spins with a conserved direction during swimming in 3D

Corkidi G.[1*], Montoya F.[1], González-Cota A.L.[2], Hernández-Herrera P.[3], Bruce N.C.[4], Bloomfield-Gadêlha H.[5*], Darszon A.[2*]

[1]Laboratorio de Imágenes y Visión por Computadora, Departamento de Ingeniería Celular y Biocatálisis, [2]Departamento de Genética del Desarrollo y Fisiología Molecular, y [3]Laboratorio Nacional de Microscopía Avanzada, Instituto de Biotecnología, Universidad Nacional Autónoma de México, Cuernavaca, 62210, México; [4]Instituto de Ciencias Aplicadas y Tecnología, Universidad Nacional Autónoma de México, Circuito Exterior S/N, Ciudad Universitaria, 04510, Ciudad de México, México; [5]Department of Engineering Mathematics & Bristol Robotics Laboratory, University of Bristol, UK.

***Corresponding authors:**
Emails: gabriel.corkidi@ibt.unam.mx, hermes.gadelha@bristol.ac.uk;
alberto.darszon@ibt.unam.mx

Abstract

In human sperm, head spinning is essential for sperm swimming and critical for fertilization. Measurement of head spinning has not been straightforward due to its symmetric head morphology, its translucent nature and fast 3D motion driven by its helical flagellum movement. Microscope image acquisition has been mostly restricted to 2D single focal plane images limited to head position tracing, in absence of head orientation and rotation in 3D. To date, human sperm spinning has been reported to be mono or bidirectional, and even intermittently changing direction. This variety in head spinning direction, however, appears to contradict observations of conserved helical beating of the

bioRxiv preprint doi: https://doi.org/10.1101/2022.11.28.517870; this version posted November 29, 2022. The copyright holder for this preprint (which was not certified by peer review) is the author/funder. All rights reserved. No reuse allowed without permission.

human sperm flagellum. Here, we reconcile these observations by directly measuring the head spinning movement of freely swimming human sperm with multi-plane 4D microscopy. We show that 2D microscopy is unable to distinguish the spinning direction in human sperm. We evaluated the head spinning of 409 spermatozoa in four different conditions: in non-capacitating and capacitating solutions, for both aqueous and viscous media. All spinning spermatozoa, regardless of the experimental conditions spun counterclockwise (CCW) as seen from head-to-tail. Head spinning was suppressed in 57% of spermatozoa swimming in non-capacitating viscous media, though, interestingly, they recovered the CCW spinning after incubation in capacitating conditions within the same viscous medium. Our observations show that the spinning direction in human sperm is conserved, even when recovered from non-spin, indicating the presence of a robust and persistent helical driving mechanism powering the human sperm flagellum, thus of critical importance in future sperm motility assessments, human reproduction research and microorganism self-organised swimming.

Introduction

Mammalian spermatozoa invariably spin as they freely swim through a fluid. Similarly to a drill, coordinated helical motion of its whip-like flagellum causes the sperm to “corkscrew” into the fluid, causing the sperm head to spin around its longitudinal axis during locomotion (David et al., 1981; Denehy et al., 1975; Ishijima et al., 1992; Linnet, 1979; Phillips et al., 1972; Rikmenspoel, 1965; Woolley, 1977). Sperm head spinning is a direct manifestation of the cyclic molecular-motor activity shaping the flagellum into a helical beat in 3D (Woolley, 1977; Woolley et al., 1984): a right-handed helical flagellum causes the sperm head to spin clockwise (CW) whilst a left-handed sperm spins in the opposite direction when seen from head-to-tail. Sperm spinning is suppressed if the flagellar waveform is

bioRxiv preprint doi: https://doi.org/10.1101/2022.11.28.517870; this version posted November 29, 2022. The copyright holder for this preprint (which was not certified by peer review) is the author/funder. All rights reserved. No reuse allowed without permission.

purely planar (2D), as observed for human sperm penetrating viscous medium (Smith et al., 2009). The spinning ability has also been reported to be critical for a successful fertilization, related to a complex cascade of trans-membrane ion channel transport that coordinates this mode of motion (Miller et al., 2018; Zhao et al., 2022). Head spinning is thus a fundamental feature linking the molecular workings of the flagellar beat with sperm motion, and thus an important proxy of symmetry, or rather symmetry-breaking, of the helical flagellar movement in 3D (Zaferani et al., 2021).

For the past 50 years researchers have attempted to quantify and define the spinning direction of the human sperm head, though, until now, there is no consensus in the literature of its spinning directionality. Human sperm spinning has been observed to be mono-directed (Linnet, 1979; Smith et al., 2009b; Phillips, 1983; Woolley, 1977), bi-directed (Ishijima et al., 1992; Dardikman-Yoffe et al., 2020; Drake, 1974), and even intermittently directed (Bukatin et al., 2015). However, such reported variety in spinning direction appears to contradict observations of a conserved helical beating of human sperm flagellum (Bukatin et al., 2015; Ishijima et al., 1992; Linnet, 1979; Powar et al., 2022; Zhao et al., 2022), and conserved chirality of structural components in mammalian sperm flagella (Fawcett, 1975; Leung et al., 2021), with no agreement as to the direction of rotation reported in earlier studies (Woolley, 1977; Bishop, 1958; Drake, 1974; Yeung and Woolley, 1984; Woolley, 1979; Blokhuis, 1961; Daloglu et al., 2018).

The human sperm head is translucent and has an axis-symmetric morphology around its spinning axis (Figure 1), making it prone to optical illusions that may obscure accurate detection of its spinning directionality. As such, the sperm head is prone to perception bistability which can further disguise the true spinning direction in translucent objects (Liu et al., 2012). This optical illusion causes spinning translucent objects to appear to oscillate

bioRxiv preprint doi: https://doi.org/10.1101/2022.11.28.517870; this version posted November 29, 2022. The copyright holder for this preprint (which was not certified by peer review) is the author/funder. All rights reserved. No reuse allowed without permission.

back-and-forth or spin with a switchable, and thus undefined, direction (Liu et al., 2012). At microscale this difficulty is augmented by the contrast inversion effect due to spherical aberrations in microscope objectives that cause a contrast-switch depending on the object's relative position to the plane of focus (Keller et al., 2022; Goodman, 2005). Switching the contrast of spinning objects and its subsequent dependence on the focal plane used for imaging, have unknown consequences on the detected direction of spinning (Figure 2), as we further detail in this paper. Altogether, these challenges indicate that 2D microscopy may not provide accurate measurement of the directionality of sperm head spinning (Muschol et al., 2018). Incidentally, *direct* detection of the head spinning direction in human sperm has been limited thus far to single-plane 2D microscopy. Indirect detection methods either exploit the sperm head centre-position traces (Ishijima et al., 1992) or flagelloid tracks in 3D (Ishijima et al., 1992; Bukatin et al., 2015; Dardikman-Yoffe et al., 2020), by following the trajectory of a certain point along the flagellum. In this case, the head spinning direction is assumed to follow similar rotational movement of the position traces of these counterparts. Indirect detection studies however have not yet been validated against direct measurements of head spinning, as no ground truth is available for this, highlighting this is an urgent gap in literature. Furthermore, different rotations are present during sperm swimming and it is a challenging task to infer head spinning indirectly from flagellar tracks that rotate around an average swimming axis, or from flagelloid tracers that are ill posed and cannot define robustly a common rotation point. Indeed, no modern 3D flagellar tracking research has attempted to directly track the head spinning direction in human sperm. This is, however, critical for understanding sperm swimming as human sperm precesses around its swimming axis: the sperm head spins at the same time that the cell as a whole rotates around its swimming direction.

bioRxiv preprint doi: https://doi.org/10.1101/2022.11.28.517870; this version posted November 29, 2022. The copyright holder for this preprint (which was not certified by peer review) is the author/funder. All rights reserved. No reuse allowed without permission.

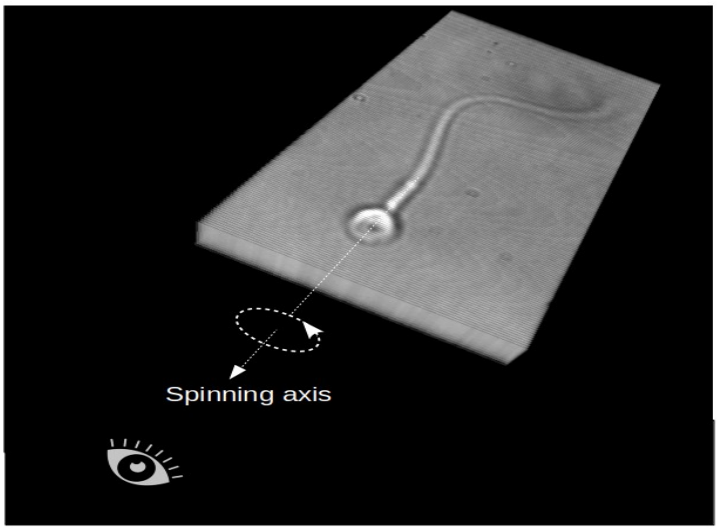

Figure 1. The human sperm head is translucent and has an axis-symmetric morphology around its spinning axis. The reference of observation in this work is from head to tail.

bioRxiv preprint doi: https://doi.org/10.1101/2022.11.28.517870; this version posted November 29, 2022. The copyright holder for this preprint (which was not certified by peer review) is the author/funder. All rights reserved. No reuse allowed without permission.

Here we solve this half-century old problem using a high-resolution multi-plane 4D method (Corkidi et al., 2008; Silva-Villalobos et al., 2014; Pimentel et al., 2012; Corkidi et al., 2021; Gadêlha et al., 2020; Hernández et al., 2022) to directly detect the head spinning direction of human spermatozoa. This method employs 4D bright-field microscopy with a 100x high-magnification objective that scans a 3D volume with high-speeds as sperm spin and swim through the fluid. The high-precision 4D microscopy described here provides a dense stack of multiple focal planes that bypass limitations of: (i) 2D microscopy that only uses a single focal plane, (ii) the image dependence on focal plane positioning, (iii) difficulties arising from contrast-switch of spherical aberrations of the lens, and (iv) perception bistability effect of translucent spinning objects. We additionally show that head sperm spinning direction cannot be confidently deduced from a single focal plane imaging. We analyzed over 400 free-swimming human spermatozoa in four different conditions, using capacitating and non-capacitating solutions within aqueous and viscous media. 100% of all sperm heads were observed to spin counterclockwise (CCW) when viewed from head-to-tail, Figure 1. Our observations show that the spinning direction in human sperm is conserved, even when head spinning is recovered from planar beating, indicating the presence of a persistent helical driving mechanism powering the human sperm flagellum. These observations may have important implications concerning the internal machinery driving the head spinning, flagellum-powered cell motility and its physiology.

RESULTS

a) 2D single-plane imaging cannot inform confidently the direction of head spin

bioRxiv preprint doi: https://doi.org/10.1101/2022.11.28.517870; this version posted November 29, 2022. The copyright holder for this preprint (which was not certified by peer review) is the author/funder. All rights reserved. No reuse allowed without permission.

Classical 2D single-plane imaging is not suitable to establish confidently the direction of the head spin. Figure 2 shows an image sequence of 17 timepoints evolving from left to right at two different focal planes containing the information of a complete head turn. As can be appreciated, the visual information in these two planes is distinct and complex, with changes in the brightness, contrast switches and head position relative to the focal plane. Establishing the head spinning direction is not possible using single-plane information alone (see Video 1). Visual inspection by different observers leads to different spinning directions due to bistability perception.

bioRxiv preprint doi: https://doi.org/10.1101/2022.11.28.517870; this version posted November 29, 2022. The copyright holder for this preprint (which was not certified by peer review) is the author/funder. All rights reserved. No reuse allowed without permission.

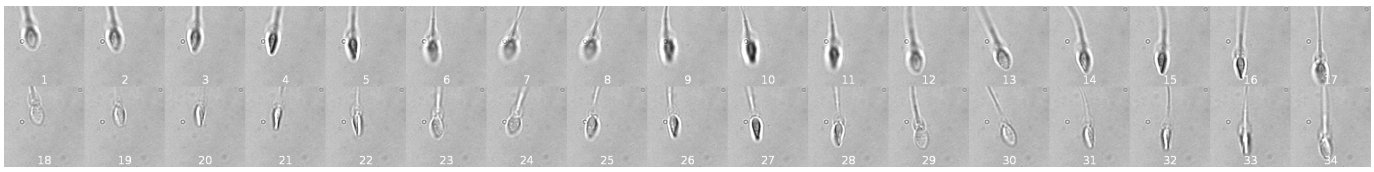

Figure 2. Image sequence of 17 timepoints at two different focal planes separated by 4.8 microns (image 1-17 upper focal plane, images 18-34 lower focal plane), containing the information of a complete head turn (see Video 1).

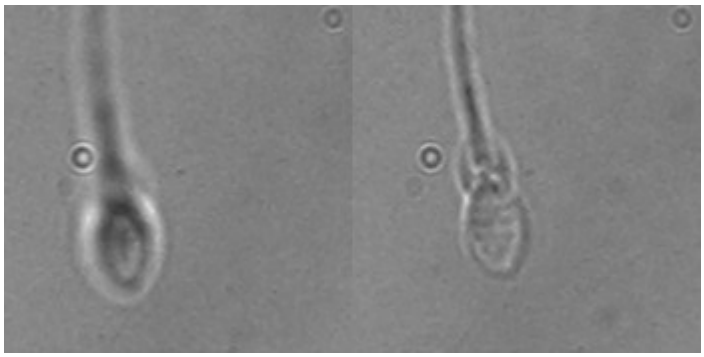

Video 1. Establishing the head spinning direction is not possible using single-plane information alone. Visual inspection by different observers leads to different spinning directions due to bistability perception.

bioRxiv preprint doi: https://doi.org/10.1101/2022.11.28.517870; this version posted November 29, 2022. The copyright holder for this preprint (which was not certified by peer review) is the author/funder. All rights reserved. No reuse allowed without permission.

b) 3D bright field image stacks acquisition and contrast inversion for the human sperm head.

Figure 3 shows 25 consecutive focal planes (out of 50) from a single piezo rising slope and assumed to correspond to a single instant. The experimental setup provides a temporal resolution of 1/160 seconds and a spatial resolution along the *z* direction of 0.4 μm. In this figure, different head elements and their contrast-inversion are revealed as the focal plane moves through the sperm head, appearing as bright pixels inside the head with a dark halo outside to the head behind the focal plane (Figure 3(1)), and as dark pixels inside the head with a bright halo outside to the head in front of the focal plane (Figure 3(25)). Note particularly how the left narrowest sides of the sperm head begin to appear as a bright white border (as detailed in the next sub-sections) when images move farther from the objective lens (15 to 11) in Figure 3. This contrast inversion effect will be explored in the following section to track head spin directionality.

bioRxiv preprint doi: https://doi.org/10.1101/2022.11.28.517870; this version posted November 29, 2022. The copyright holder for this preprint (which was not certified by peer review) is the author/funder. All rights reserved. No reuse allowed without permission.

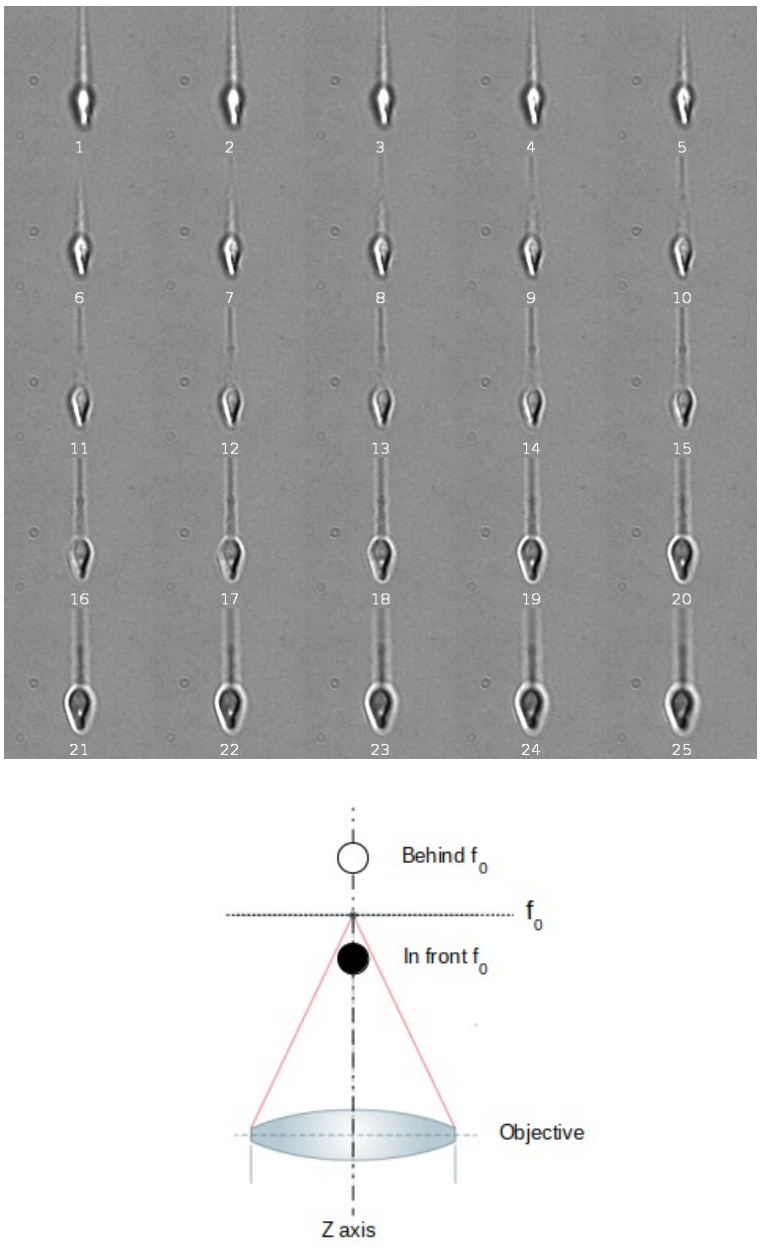

Figure 3. Multifocal plane acquisition. From left to right and top to bottom, this figure shows 25 consecutive focal planes (out of 50) acquired while the piezoelectric device is rising. Frames (150 x 150 pixels each) were cropped, for visualization purposes, from 640 x 480 pixels image sequences. Each focal plane is separated by 0.4 μm respectively (see Materials and Methods). The schematic at the bottom depicts how the spherical aberration of the optical system produces a contrast inversion over translucent objects depending on

bioRxiv preprint doi: https://doi.org/10.1101/2022.11.28.517870; this version posted November 29, 2022. The copyright holder for this preprint (which was not certified by peer review) is the author/funder. All rights reserved. No reuse allowed without permission.

their position with respect to the focal plane f_0. The object appears dark if placed in front of the focal plane f_0, while bright if placed behind.

bioRxiv preprint doi: https://doi.org/10.1101/2022.11.28.517870; this version posted November 29, 2022. The copyright holder for this preprint (which was not certified by peer review) is the author/funder. All rights reserved. No reuse allowed without permission.

c) Contrast inversion of the sperm head is due to the spherical aberration of the objective lens using bright-field microscopy.

The Rayleigh-Sommerfeld back propagation reconstruction method has been commonly used to reconstruct the sperm flagellum in 3D (Bukatin et al., 2016), but this is based solely on diffraction and cannot distinguish between defocus before or after the focused object plane (Lee et al., 2007). Usually, the contrast inversion of the defocused object is used heuristically to post process the results of the back-propagation method to produce a final reconstructed object (Lee et al., 2007), alternatively, phase information from the reconstructed object can be used to post-process the reconstruction itself (Wilson et al., 2012). It is well known that microscope objectives are extremely well corrected for conjugate planes, which are focused objects and image planes, but this is not true for non-conjugate planes. Aberrations, particularly spherical aberrations, can strongly contribute to image quality for non-conjugate planes (Keller et al., 2022; Kidger, 2002). Here we demonstrate that it is the spherical aberration of the objective lens that produces a contrast inversion as a function of the position of the object relative to the focused object plane (Figure 3).

Diffraction effects that appear in the point spread function (PSF) are given by the Fourier transform of the lens aperture function multiplied by the aberration function,

$$PSF = \boldsymbol{F}\left(P(x,y)\exp\left(ikW(x,y)\right)\right), \qquad (1)$$

where $\boldsymbol{F}()$ is the Fourier transform in the lens aperture plane, (x,y) is the position in the image plane, $P(x,y)$ is the lens pupil (almost always taken as a circle), $k = 2\pi/\lambda$ is the light wave number, and $W(x,y)$ is the wave aberration function given by (Goodman, 2005)

bioRxiv preprint doi: https://doi.org/10.1101/2022.11.28.517870; this version posted November 29, 2022. The copyright holder for this preprint (which was not certified by peer review) is the author/funder. All rights reserved. No reuse allowed without permission.

$$W(x,y)=A_d\frac{x^2+y^2}{r^2}+A_s\left(\frac{x^2+y^2}{r^2}\right)^2, \qquad (2)$$

where A_d is the amplitude of the defocus, A_s is the amplitude of the spherical aberration, and r is the radius of the lens pupil. The first term in Equation 2 is the defocus contribution, and the second term is the contribution of the spherical aberration. One important aspect is the sign of the defocus term. From Goodman 2005, using the Gauss equation for a defocused system we have:

$$\frac{1}{d_0}+\frac{1}{d_i}=\frac{1}{f}\rightarrow\frac{1}{d_0}+\frac{1}{d_i}-\frac{1}{f}=-A_d, \qquad (3)$$

so that $A_d=0$ when the system is focused. Given that f and d_i (focal length and the distance from the lens to the image) are fixed, and the distance from the object to the lens (d_0) changes when the optical system is defocused, when d_0 increases (the object is further away from the objective lens), the term $\frac{1}{d_0}+\frac{1}{d_i}$ is smaller and $A_d>0$. When d_0 decreases (the object is closer to the objective lens), the term $\frac{1}{d_0}+\frac{1}{d_i}$ increases and $A_d<0$.

We assume that the spherical aberration has the same sign for a defocus below and above the geometrical focal plane. Simulations for a rectangular object are shown in Figure 4. The diffraction from defocus alone in Figure 4A and B, does not give an inversion of contrast between the object positions below and above the focused object plane. Figure 4C and D, however, where a small spherical aberration contribution has been included, does show the contrast inversion effect. Finally, Figure 4E shows the case of an inclined object where the left part of the object is further away from the objective lens and the right

bioRxiv preprint doi: https://doi.org/10.1101/2022.11.28.517870; this version posted November 29, 2022. The copyright holder for this preprint (which was not certified by peer review) is the author/funder. All rights reserved. No reuse allowed without permission.

253 part is closer to the objective lens, showing the contrast inversion within the object. It is
254 important to note that a change in sign of the spherical aberration contribution changes the
255 contrast inversion: with $A_s>0$ an object closer to the objective lens than the focused
256 object plane would be dark and an object further from the objective lens would be bright.
257 The sign of the aberration depends on the specific design of the optical system and so
258 could vary between different laboratories working with different objectives. Our simulations
259 consider a spherical aberration within the range of the optical system used in our
260 experiments.
261
262 The contrast-switch inside the object is a direct manifestation of the object's inclination
263 relative to the objective lens (Figure 4E). Here we exploit for the first time this unique
264 optical effect to extract the directionality of a spinning object, such as the sperm head, as
265 detailed below. Figure 5 shows how this contrast-switch of its planar projection varies
266 when the inclination of the object increases as the object spins around its long axis.
267 Clockwise spinning causes the bright part (further away from the objective lens, see white
268 arrows) of the inclined object to always move from right-to-left and the dark part to move
269 from left-to-right (dark arrows), whilst counterclockwise spinning causes the bright region
270 to always move from left-to-right and at the same time that the dark region moves from
271 right-to-left. Once a half-cycle is completed, and the flat object is parallel to the objective
272 lens, the bottom part of the object reaches the top and vice versa, re-setting the contrast
273 inversion: any part of the object reaching the top appears as bright, likewise any part of the
274 object reaching the bottom will appear as dark. In other words, after a half-cycle, a
275 bright/dark region abruptly re-appears at starting location, after reaching the end of the
276 object on the opposite side. For this reason, if an object spins in the same direction, this
277 will be manifested in the image as the bright or dark regions of the objects moving with a

bioRxiv preprint doi: https://doi.org/10.1101/2022.11.28.517870; this version posted November 29, 2022. The copyright holder for this preprint (which was not certified by peer review) is the author/funder. All rights reserved. No reuse allowed without permission.

278 persistent direction relative to the object's orientation (left-to-right or right-to-left). Likewise,
279 if the object spinning direction is reversed, the direction of motion of bright/dark regions will
280 equally reverse relative to the object's orientation (right-to-left or left-to-right). The
281 spherical aberration effect causing the contrast switch within the object's image allows for
282 robust, and yet simple, detection of spinning direction of axis-symmetric objects, such as
283 the human sperm head demonstrated below, that otherwise would not be possible, and
284 this feature is exploited here for the first time.

bioRxiv preprint doi: https://doi.org/10.1101/2022.11.28.517870; this version posted November 29, 2022. The copyright holder for this preprint (which was not certified by peer review) is the author/funder. All rights reserved. No reuse allowed without permission.

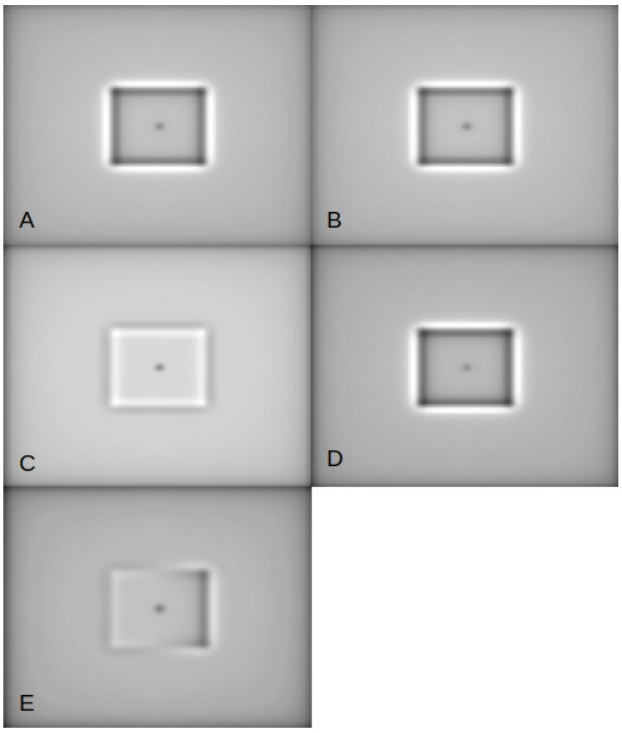

Figure 4. Results of the simulation of image formation for a weakly scattering phase object. (A) image with $A_s=0$ and $A_d=0.3$; (B) image with $A_s=0$ and $A_d=-0.3$; (C) image with $A_s=-0.0004$ and $A_d=0.04$; (D) $A_s=-0.0004$ and $A_d=-0.04$; (E) image for an inclined planar object with $A_s=-0.0004$. The centre of the object plate is in the focused object plane of the lens and the right part of the object is closer to the objective lens.

bioRxiv preprint doi: https://doi.org/10.1101/2022.11.28.517870; this version posted November 29, 2022. The copyright holder for this preprint (which was not certified by peer review) is the author/funder. All rights reserved. No reuse allowed without permission.

312

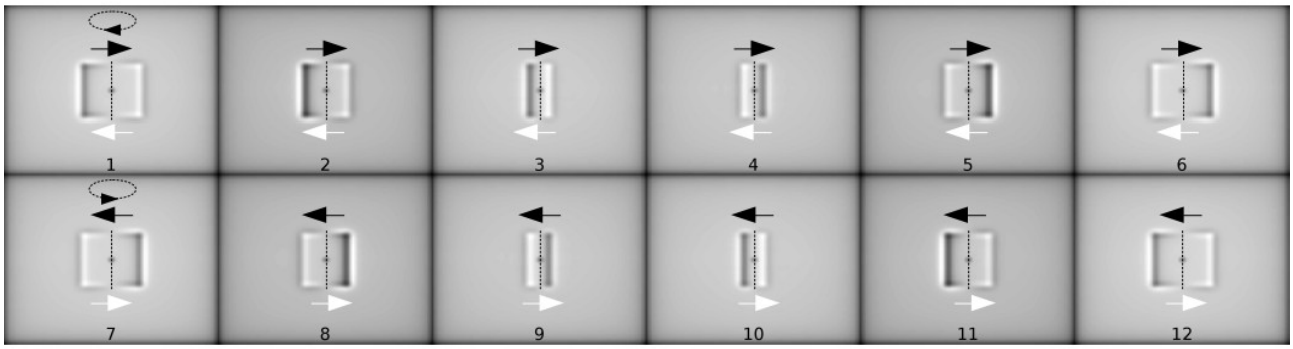

313 Figure 5. Simulation results of a spinning object, showing the direction of movement of the
314 dark and bright left/right edges from 2D imaging from a fixed focal plane projection. Top:
315 (images 1 to 6) a clockwise rotation viewed from the top of the images; bottom: (images 7
316 to 12) a counterclockwise rotation. A_s=-0.004 and the maximum defocus is A_d=±0.2.

bioRxiv preprint doi: https://doi.org/10.1101/2022.11.28.517870; this version posted November 29, 2022. The copyright holder for this preprint (which was not certified by peer review) is the author/funder. All rights reserved. No reuse allowed without permission.

d) Bright region induced by sperm head inclination moves with head spinning.

The human sperm head has a flattened side, and when the head spins around its longitudinal axis, the narrow side behind the focal plane is clearly seen as a bright region, whilst the part of the head above the focal plane appears as dark, when the sperm head is inclined relative to the objective lens (Figure 6, images 4-6, see arrows). The contrast switch inside the sperm head is due to the head inclination relative to the objective lens (images 4-6); when the sperm head is parallel to the objective lens, no switch in contrast occurs (images 8-9), as demonstrated in the above section. The time-sequence in Figure 6 (images 4-7), shows the bright region moving from left-to-right relative to the sperm head orientation due to changes in inclination of the sperm head caused by the head spinning. This switch in contrast when the head is inclined is barely perceptible when observed with 2D microscopy (Figure 2), as the sperm head continuously changes its position relative to the focal plane when swimming freely in the fluid (see Video 1). A minimal focal change at the micron scale is sufficient to prevent the detection of bright-dark regions induced by the sperm head inclination, as shown in Figure 4E. Indeed, Figures 2 and 6 show the inversion in contrast due to inclination of the sperm head is clearly visible for only a few focal planes as the piezo rises. It would be a challenging task to change a single focal plane dynamically, at the microscale, to keep the sperm head exactly in focus to enable the detection of this change in contrast optical effect across the head using 2D microscopy, as shown in Figure 5. Our multifocal system bypasses this challenge and allows unique detection of the accumulated changes in contrast from bright-to-dark regions induced by the sperm head inclination from a stack of multiple focal planes (Figure 3), as detailed below.

bioRxiv preprint doi: https://doi.org/10.1101/2022.11.28.517870; this version posted November 29, 2022. The copyright holder for this preprint (which was not certified by peer review) is the author/funder. All rights reserved. No reuse allowed without permission.

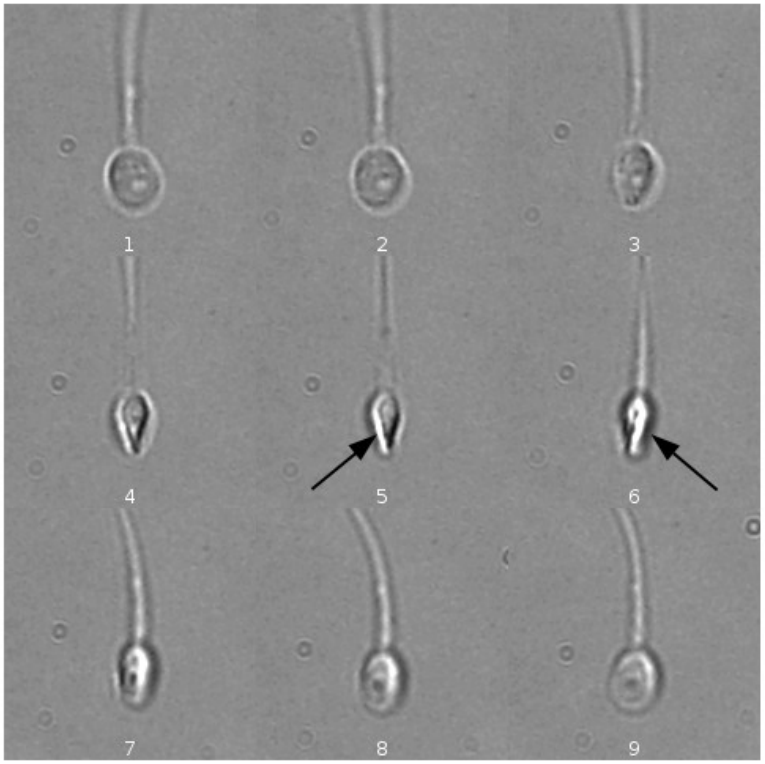

Figure 6. The contrast inversion optical effect during a half turn of a sperm head. Nine consecutive timepoints where the contrast inversion optical effect is clearly observed (same focal plane), i.e. the narrowest, focally lower, border of the sperm head (behind the focal plane) is enhanced resulting in a bright border while the sperm head is inclined during head spinning (highlighted with arrows).

bioRxiv preprint doi: https://doi.org/10.1101/2022.11.28.517870; this version posted November 29, 2022. The copyright holder for this preprint (which was not certified by peer review) is the author/funder. All rights reserved. No reuse allowed without permission.

e) Validation of the sperm head spinning detection using contrast switch of the sperm head.

We validated the use of the contrast inversion of the sperm head shown previously to detect the head spinning direction against direct tracking of the motion of a particle attached to a sperm neck during head spinning. Figure 7 shows a sperm cell with such a particle rigidly attached to its neck, whilst spinning 360 degrees during free-swimming motion. In the time-sequence for the Figure 7A, the focal plane is approximately placed between the sperm and the particle along *z*, in such a way that when this particle is behind the focal plane (images 1-4), it appears as bright, while when the particle is in front of the focal plane (images 5-8), it appears as dark. The arrow on the particle shows the direction of the displacement during head spinning; the black arrow indicates that the particle is behind the focal plane (bright particle), while the red arrow indicates when the particle is in front of the focal plane (dark particle). As such, the particle rotates in the CCW direction following the sperm head spinning motion: the particle moves from left-to-right when behind the focal plane (1-4), and moves from right-to-left when above the focal plane (5-8). On the other hand, the bright border arising from the contrast inversion when the sperm head is inclined relative to the objective lens always moves in the same direction relative to the sperm head orientation, from left-to-right, as shown by the arrow on this bright region, regardless of whether the particle is above (5-8) or below (1-4) the focal plane in each of its half-cycle (see Video 2). CCW spinning (as seen from head-to-tail) causes the sperm head bright region to always move from left-to-right relative to the sperm head, in agreement with the direction of the particle rotation above.

When the focal plane is placed between the particle and the flagellum (Figure 7B), it becomes evident their relative position: in the sequence 1-2 (top images), the particle (bright) is located behind the flagellum (dark) while moving to the right, while in the

bioRxiv preprint doi: https://doi.org/10.1101/2022.11.28.517870; this version posted November 29, 2022. The copyright holder for this preprint (which was not certified by peer review) is the author/funder. All rights reserved. No reuse allowed without permission.

372 sequence 3-4, the particle is in front (while moving to the left). The movement direction of
373 the particle, combined with its relative position to the flagellum makes to confidently
374 conclude a CCW spin.
375
376
377
378
379
380
381
382

383
384 Video 2. A sperm cell with a translucid particle rigidly attached to its neck, whilst spinning
385 360 degrees during free-swimming motion.

bioRxiv preprint doi: https://doi.org/10.1101/2022.11.28.517870; this version posted November 29, 2022. The copyright holder for this preprint (which was not certified by peer review) is the author/funder. All rights reserved. No reuse allowed without permission.

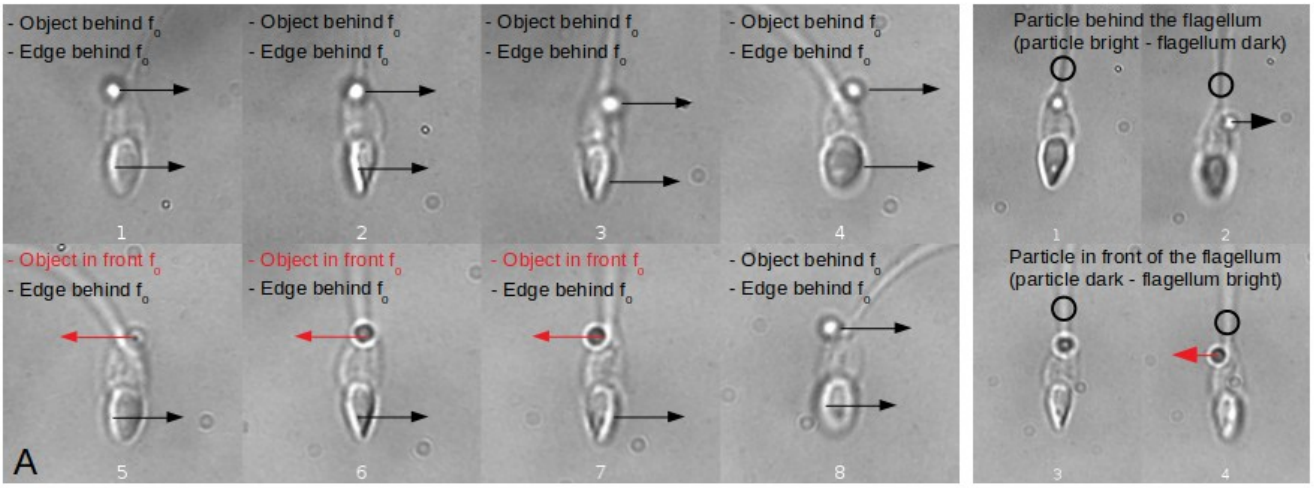

386 Figure 7. Tracking a translucent particle stuck on a spermatozoon's neck, presenting the
387 contrast inversion optical effect while turning 360 degrees with a free-swimming sperm. (A)
388 Focal plane between Particle and Bright border: when the particle is above the
389 spermatozoon's neck it appears bright (behind the focal plane), while appearing dark when
390 under the neck (in front of the focal plane); simultaneously, the border of the spermatozoon
391 is always behind the focal plane appearing bright, showing a CCW spin direction when
392 seen from head-to-tail. Note the change of direction of the particle when it is dark, as the
393 particle rigidly follows the head spinning. (B) Focal plane between Particle and Flagellum:
394 when the focal plane is placed between the particle and the flagellum, it becomes evident
395 their relative position: in the sequence 1-2 (top images), the particle (bright) is located
396 behind the flagellum (dark) while moving to the right, while in the sequence 3-4, the
397 particle is in front (while moving to the left). A CCW spin is evident from these images. This
398 shows that the proposed method is capable of detecting spinning directions.

bioRxiv preprint doi: https://doi.org/10.1101/2022.11.28.517870; this version posted November 29, 2022. The copyright holder for this preprint (which was not certified by peer review) is the author/funder. All rights reserved. No reuse allowed without permission.

f) Detection of sperm head spin direction from multifocal stacks

Here, we exploit the volume stack and accumulate the contrast-switch caused by the head inclination occurring at different focal planes by integrating this multifocal plane information in a single image. This circumvents the fact that the contrast switch across the sperm head is only observable for a few focal planes, as shown above. To this purpose, we calculated a 2D Maximum Intensity Projection (MIP) image (Schindelin et al., 2012) for each piezo rising slope *z* stack containing 50 focal planes through the whole acquisition time of 3.5 sec. The 2D MIP of the z-stack accumulates in a single image the maximum values of all the focal planes, i.e. bright regions in the image shown in Figure 6 for a time sequence. The integrated bright region induced by the switch in contrast when the sperm head is inclined is manifested as a superimposed one-sided halo, only present when the sperm head is inclined relative to the objective lens (images 4-7). Figure 8 shows the accumulated bright region moving from left-to-right relative to the head as time progresses from time sequence 4-7 (see also Video 3). The motion of the accumulated MIP bright feature over the course of time follows the direction of head spinning, as demonstrated in previous sections.

bioRxiv preprint doi: https://doi.org/10.1101/2022.11.28.517870; this version posted November 29, 2022. The copyright holder for this preprint (which was not certified by peer review) is the author/funder. All rights reserved. No reuse allowed without permission.

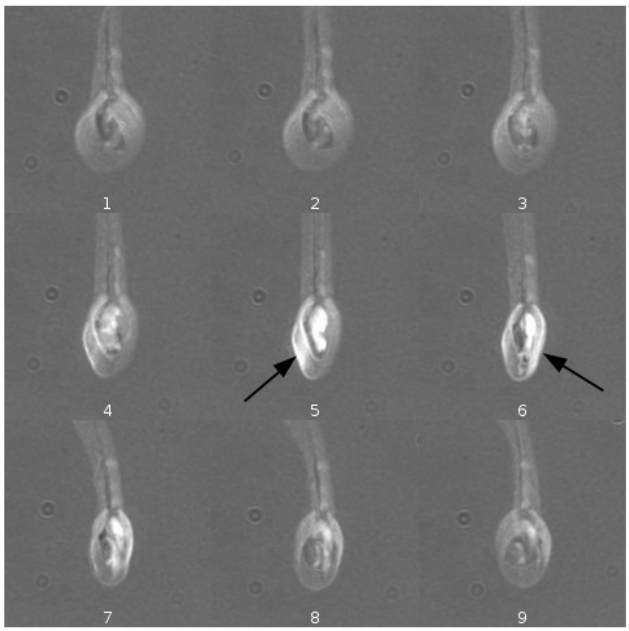

Figure 8. 2D MIP's (Maximum Intensity Projections) of 9 consecutive piezo rising slopes -timepoints- (50 images each projection, images 1 to 9) during a half turn of a sperm head (left to right, top to bottom). The brightest pixels over the z axis from 50 images corresponding to one half cycle of the piezo device are projected into a single plane to integrate the spherical aberration spread over the z range. The bright region moves from left-to-right relative to the sperm head (arrows) (See Video 3).

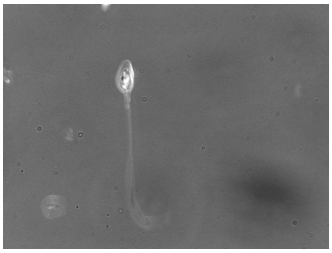

Video 3. The 2D MIP of the z-stack accumulates in a single image the maximum values of all the focal planes, i.e. bright regions for a time sequence. A bright region moves from right-to-left relative to the head as time progresses. At the final part of the video, another spermatozoon appears swimming in the opposite direction, showing the bright region to move consistently in the inverse direction (see also Supporting Information and Figure S1).

bioRxiv preprint doi: https://doi.org/10.1101/2022.11.28.517870; this version posted November 29, 2022. The copyright holder for this preprint (which was not certified by peer review) is the author/funder. All rights reserved. No reuse allowed without permission.

The directional motion of the superimposed bright regions is extracted from the variations on the intensity profile moving along the segment ***bb'*** (red line shown in Figure 9). To detect the direction of the movement in which the one-side bright halo moves with respect to the longitudinal axis of the head (as placed in front of the head -viewing the sperm from the tip of the head to the flagellum-, line **C** Figure 9A), we have employed the following steps:

1) To track the sperm head position, we used the method described in (Corkidi et al., 2021). This method provides the spermatozoa dominant orientation over time (angle ϕ in Figure 9A) relative to the microscope fixed frame of reference, depicted by the line **C**. The center of the sperm head over line **C** is defined as a. These two experimental parameters define the position and orientation of the major axis of the sperm head represented by **C** (see Corkidi et al., 2021). By construction, **C'** is perpendicular to **C**, and the intersection point is at a distance of d μm from a (1/3 the average size of the long axis of the human sperm head). Finally, ***b*** and ***b'*** are located symmetrically along **C'** at a distance ***b*** from the intersection of **CC'**. The pixels along ***bb'*** (represented by the red line) are used to measure the intensity profile over the 2D MIP image (see Video 4). The direction of motion of the maximum intensity of the profile series (by using variation in position of the weighted average -see next section- along the segment bb', as shown in Figure 9C and D) defines the sperm head spin direction. The equation describing the points along the line **C** is $y=(tan\phi)x+(y_a-x_a tan\phi)$, the intersection point between **C** and **C'** is given by the condition $d=\sqrt{(x-x_a)^2+(y-y_a)^2}$ and its coordinates (x_d, y_d). The equation describing the points along **C'** is defined by $y'=(\frac{-1}{tan\phi})x'+(y_d+\frac{x_d}{tan\phi})$. The points ***b*** and ***b'*** are positioned at

bioRxiv preprint doi: https://doi.org/10.1101/2022.11.28.517870; this version posted November 29, 2022. The copyright holder for this preprint (which was not certified by peer review) is the author/funder. All rights reserved. No reuse allowed without permission.

distances $b = \pm\sqrt{(x'-x_d)^2+(y'-y_d)^2}$ along **C'** centered at the intersection with **C**. The set of points that are embedded in the ***bb'*** segment are $\{\vec{r}_i\}_{i=1}^{N}$, where N is the number of points belonging to ***bb'*** (red line in Fig 9.). From this, the gray level profile over the segment ***bb'*** can be quantified.

2) Determination of the sperm head spinning direction.

The position of weighted average of each intensity profile along ***bb',*** while the head is turning, is quantified to establish the head spin direction. The weighted average position over ***bb'*** is $\vec{r}_{wa}$, analogous to the "center of mass" of the intensity levels along ***bb'***. Tracking $\vec{r}_{wa}$ over time reveals the movement of the brightest part of the sperm head 2D MIP. This feature applied to the gray level profile over the line segment ***bb'*** (see Figure 9) is expressed as: $\vec{r}_{wa} = \frac{\sum_{i=1}^{N} I_{MIP,i}\vec{r}_i}{\sum_{i=1}^{N} I_{MIP,i}}$, where $I_{MIP,i}$ is the gray level value of the corresponding 2D MIP image $\vec{r}_i$. If $\vec{r}_{wa}$ moves from ***b*** to ***b'*** the cell is rotating CCW and otherwise CW, as shown in Figures 5 and 9.

Figure 9A and B shows the segment ***bb'*** positioned over the sperm head in two consecutive time points with the bright border moving from ***b*** to ***b'***. The corresponding gray level of the 2D MIP profile is plotted at the bottom of each image in C-D. Figure 9E shows the values of the weighted average for two and a half head turns as shown in Video 3 and Video 4. Red circles over the first minimum and maximum correspond to the first half turn. Minima denote that the weighted average of the intensity profile is shifted towards the ***b*** side of the sperm head (taking ***b*** (from ***bb'***) as the origin for the profile), while maxima

bioRxiv preprint doi: https://doi.org/10.1101/2022.11.28.517870; this version posted November 29, 2022. The copyright holder for this preprint (which was not certified by peer review) is the author/funder. All rights reserved. No reuse allowed without permission.

484 denote the shift towards the opposite ***b'*** side. Figure 9F consists of the intensity profiles
485 (***bb'***) kimograph; lower dashed lines point out the bright profiles corresponding to Figures
486 A,B,C,D denoting a 180 degrees head turn. The upper time ascending arrow from left-to-
487 right of the kimograph denotes a CCW head turn.
488
489
490
491
492
493
494
495

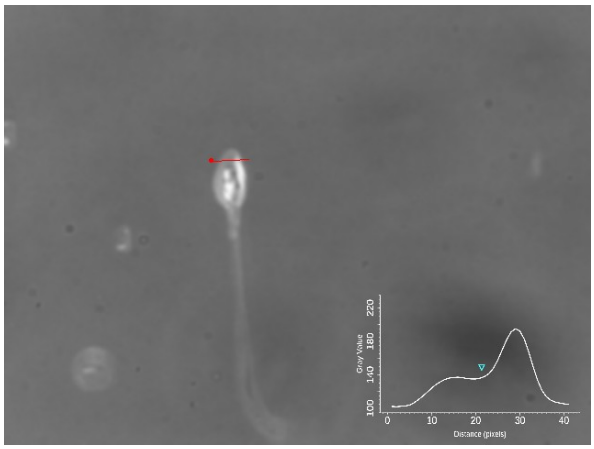

496 Video 4. Gray level of the 2D MIP profiles (over the tracked red line ***bb'*** from Figure 9) with
497 its center of mass depicted in the graph by the blue triangle.
498

bioRxiv preprint doi: https://doi.org/10.1101/2022.11.28.517870; this version posted November 29, 2022. The copyright holder for this preprint (which was not certified by peer review) is the author/funder. All rights reserved. No reuse allowed without permission.

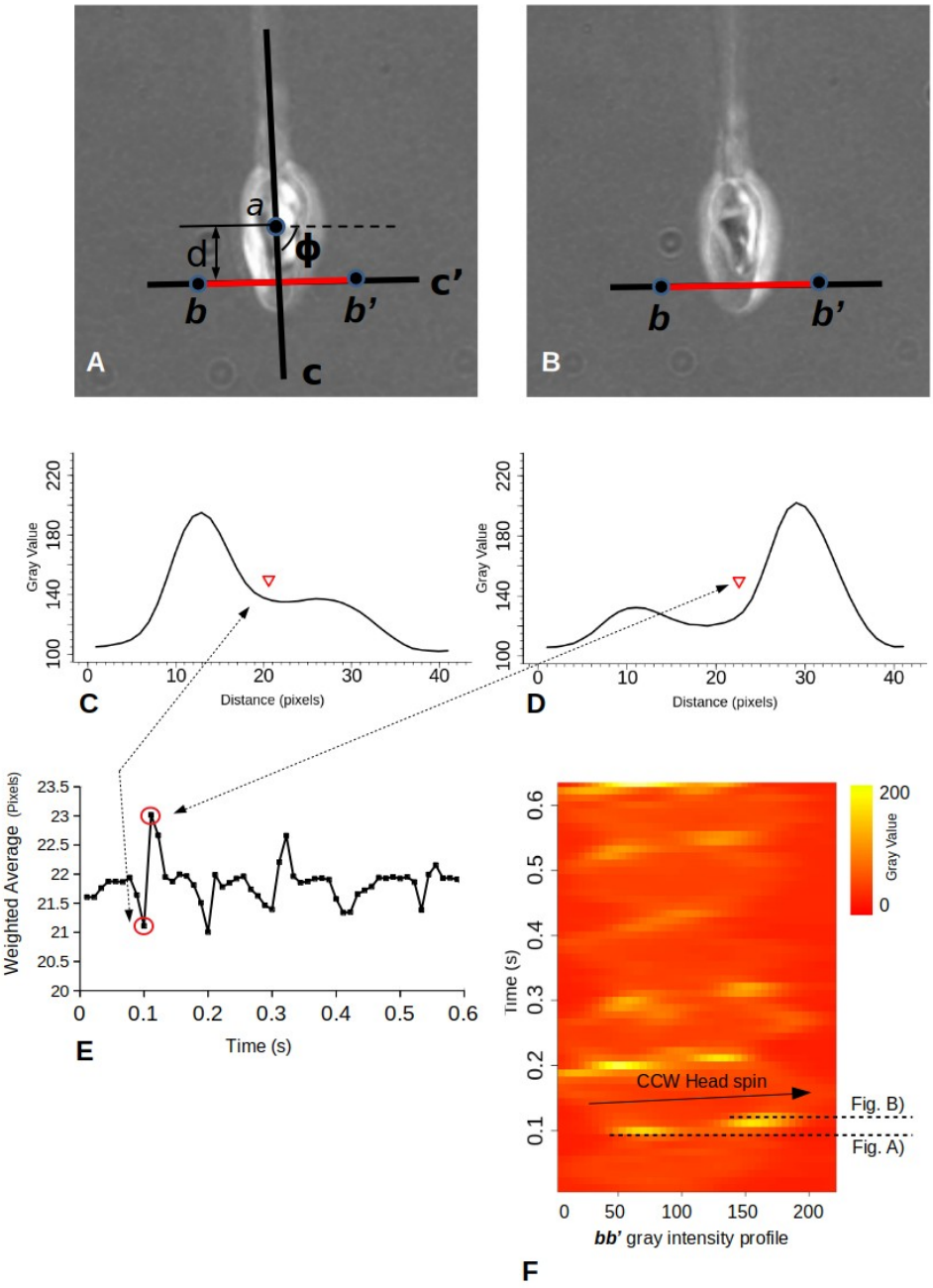

500 Figure 9. Sperm head bright region travels with a conserved direction. (A-B) The tracking
501 process estimates the angle ϕ of the dominant direction of the spermatozoon relative to
502 the microscope frame of reference and defines the orientation of the sperm (line **C**, see
503 Corkidi et al., 2021). The straight-line **C'** is perpendicular to **C**, and the intersection point is
504 at a distance of d μm from head center (1/3 the average size of the long axis of the human
505 sperm head). ***b*** and ***b'*** are located symmetrically along **C'** at a distance ***b*** from the

bioRxiv preprint doi: https://doi.org/10.1101/2022.11.28.517870; this version posted November 29, 2022. The copyright holder for this preprint (which was not certified by peer review) is the author/funder. All rights reserved. No reuse allowed without permission.

intersection of **CC'**. The coordinates of ***bb'*** (represented by the red line) are used to measure the intensity profile over the 2D MIP image (see Video 4). (C-D) The corresponding gray level of the 2D MIP profiles (from A-B) with its center of mass depicted by the red triangle. (E) Weighted average of 2D MIP profiles for two and a half head turns. Minima denote that the weighted average of the intensity profile is shifted towards the ***b*** side of the sperm head (taking ***b*** (from ***bb'***) as the origin for the profile) while maxima denote the shift towards the opposite ***b'*** side. The transition from a minimum to a maximum corresponds to half a turn of the sperm head in a CCW direction (two and a half CCW turns for this series). (F) Intensity profiles (***bb'***) kimograph; dashed lines point out the bright profiles corresponding to Figures A and B denoting a 180 degrees head turn. The lower time ascending arrow show waves of the brightness level traveling from left-to-right, indicating CCW head spin when seen from head to tail.

bioRxiv preprint doi: https://doi.org/10.1101/2022.11.28.517870; this version posted November 29, 2022. The copyright holder for this preprint (which was not certified by peer review) is the author/funder. All rights reserved. No reuse allowed without permission.

519 ***g*) Human sperm spin with a conserved counterclockwise direction.**

520 We acquired 409 human spermatozoa while freely swimming in 3D; 180 under non-
521 capacitating conditions and 229 in capacitating conditions. Both groups were studied in
522 aqueous and viscous media (see Materials and Methods). We found that in aqueous
523 media, regardless of the medium used (non-capacitating or capacitating), all the sperm
524 spun in the CCW when seen from head to tail and swimming freely. In contrast, in viscous
525 and non-capacitating medium, 57% of the analyzed sperm were not spinning at all, while
526 the remaining 43% spun in the CCW direction. Interestingly, in capacitating conditions
527 these percentages inverted: 22% of the analyzed sperm did not spin at all, whilst 78%
528 spun with the conserved CCW direction. The results summarized in Table 1 suggest that
529 capacitating media also influences the ability of sperm to spin in a viscous fluid. All human
530 sperm observed to spin did so by turning in the CCW direction when seen from head to tail
531 regardless of the experimental condition.

bioRxiv preprint doi: https://doi.org/10.1101/2022.11.28.517870; this version posted November 29, 2022. The copyright holder for this preprint (which was not certified by peer review) is the author/funder. All rights reserved. No reuse allowed without permission.

	Non capacitating media		Capacitating media	
	Aqueous	Viscous	Aqueous	Viscous
CCW	78 (100%)	65 (43%)	106 (100%)	101 (78%)
CW	0	0	0	0
No rotation	0	37 (57%)	0	22 (22%)

Table 1. Spin direction evaluation of 409 human spermatozoa while freely swimming in 3D; 180 under non-capacitating conditions and 229 in capacitating conditions (both groups in aqueous and viscous media, see Materials and Methods). All human sperm in aqueous media (non-capacitating or capacitating) spun CCW direction when seen from head to tail regardless of the experimental condition, while in viscous and non-capacitating medium, 57% of the analyzed sperm did not spin at all, while the remaining 43% spun in the CCW direction. Note that in capacitating conditions these percentages inverted: 22% of the analyzed sperm did not spin at all, whilst 78% spun with the conserved CCW direction.

bioRxiv preprint doi: https://doi.org/10.1101/2022.11.28.517870; this version posted November 29, 2022. The copyright holder for this preprint (which was not certified by peer review) is the author/funder. All rights reserved. No reuse allowed without permission.

Discussion

Sperm flagellum elastohydrodynamics, mathematical modelling and image analysis have indicated that the sperm head movement is highly dependent on the nature of forces and torques imposed by the beating flagellum and subsequent interactions with the local environment, among many other factors (Gadêlha et al., 2010; Gadêlha et al., 2019; Smith et al., 2009b; Ishimoto et al., 2017; Gaffney et al., 2011). Indeed, self-organization flagellar control models have demonstrated that mechanical attachment of the head (clamped or hinged head conditions) can even dictate the travelling wave direction of the flagellum (Riedel-Kruse et al., 2007; Camelet and Jülicher, 2020; Oriola et al., 2017; Sartori et al., 2016). These matters highlight the critical importance of directly establishing the head movement and its rotations in 3D. Furthermore, despite this critical importance and recent advances in high-speed 3D imaging and 3D microscopy, for decades there is still no consensus as to what direction human sperm spin during free-swimming motion (Muschol et al., 2018). Reports include observations of: mono-directed CW or CCW (Linnet, 1979; Smith et al., 2009b; Phillips, 1983; Woolley, 1977), bi-directed (Ishijima et al., 1992; Dardikman-Yoffe et al., 2020; Drake, 1974), and even intermittently directed head spinning (Bukatin et al., 2016). Against this background, direct detection of sperm head spinning direction and its methodology are still lacking in the literature.

Phillips, 1983 has suggested that mammalian sperm spinning direction could be easily detected with 2D bright field microscopy, by exploiting the fact that the sperm head is flattened, and thus produces blinking “flashes of light” as the head spins around its swimming axis (Phillips, 1997). It has been observed that the ‘flash of light’ travels from left-to-right when the sperm head-to-tail is aligned with the vertical axis (similarly to the sperm head orientation depicted Figure 2, and thus CW head spin was inferred. This however postulates that such ‘flash of light’ *moves in the same direction as the sperm*

bioRxiv preprint doi: https://doi.org/10.1101/2022.11.28.517870; this version posted November 29, 2022. The copyright holder for this preprint (which was not certified by peer review) is the author/funder. All rights reserved. No reuse allowed without permission.

573 *head spinning*. We have demonstrated here this to be inconsistent with direct detection of
574 the head spinning, see Figure 7. Instead, we have found that the true head spinning
575 direction is opposite to the observed left-to-right movement of this “flash of light”, which
576 similarly to Phillips, 1983 also moves from left-to-right, as depicted in Figure 7. We have
577 shown that this mismatch of movement between optical brightness and the object spinning
578 motion is accounted for by spherical aberration effects of the lens. Furthermore,
579 translucent objects, such as the sperm head, are equally prone to perception bistabilities
580 Liu et al., 2012 that equally obscure the true head spinning direction with 2D microscopy,
581 in addition to other unknown image inversions within microscopy systems (see Methods).
582 These uncertainties, together with the combined use of 2D views of the sperm’s head
583 trajectory as a proxy to derive flagellar beat information, may have significantly contributed
584 to the contradictory observations that are documented in the literature regarding the sperm
585 head spinning direction.
586 In the present study, we evaluated the head spinning direction of more than 400
587 spermatozoa. Sperm suspended under four conditions were tested: in non-capacitating
588 and capacitating solutions of normal and high viscosity. The high viscosity value was
589 chosen to emulate that of the female cervical mucus (see Methods and Suarez, 2016) and
590 sperm were incubated in capacitating media for 6 hours. One hundred percent of the
591 spinning spermatozoa, in all experimental conditions, spun CCW, as seen from head-to-
592 tail. It is important to mention that the spinning direction of each single spermatozoon was
593 evaluated for a mean time of 3.4 s. A longer temporal analysis would be desirable to
594 evaluate whether spinning direction changes over periods longer than 3 sec, though
595 unfortunately not possible with our present high-resolution 4D set-up. Taken altogether, the
596 analyzed time of the 409 free-swimming sperm totalled 23 minutes, with no directional
597 change observed. Human spermatozoa in aqueous media, independently of their

bioRxiv preprint doi: https://doi.org/10.1101/2022.11.28.517870; this version posted November 29, 2022. The copyright holder for this preprint (which was not certified by peer review) is the author/funder. All rights reserved. No reuse allowed without permission.

598 capacitation state, all spun CCW. In contrast, in high viscosity, 57 % of spermatozoa in
599 non-capacitating media did not spin at all, and interestingly most of them recovered their
600 CCW rotation (80 %) when incubated in capacitating media. This striking head spinning
601 recovery phenomenon, as well as how sperm head spinning motion and flagellar rolling
602 influence swimming trajectories in 3D remain to be fully explored.
603
604 **Conclusions**
605
606 We studied here a half-century old problem by exploiting unique switch in contrast due to
607 spherical aberration effect in brightfield microscopy. We have shown that 2D microscopy
608 alone cannot distinguish spinning direction in axis-symmetric, streamlined, translucid
609 human swimming sperm; as well, methods employing such imaging technique may need
610 reassessment, whilst no methodology are currently available to directly measure human
611 head spinning. Indeed, previous studies mostly used visual inspection from video-
612 microscopy images or indirect measurement using flagellar tracing in 3D. We showed that
613 contrast inversion can be exploited to track head spinning but this requires finding the
614 appropriate focal plane in which the sperm head is, centred exactly at the focal plane; a
615 challenging task for freely-swimming spermatozoa as the head moves up and down during
616 cell progression. This is resolved by using a multi-plane detection system. The
617 methodology was validated as coherence and consistence prevailed between optics
618 theory and direct tracking of different sperm cells with particles attached to neck and head.
619 We have observed that human sperm head spins with a robust, conserved, and
620 recoverable counterclockwise spinning direction (when viewed from head to tail). Our
621 observations reconcile structural information of mammalian sperm that observe flagellar
622 architecture with conserved chirality in the axonemal driving unit with a conserved direction

bioRxiv preprint doi: https://doi.org/10.1101/2022.11.28.517870; this version posted November 29, 2022. The copyright holder for this preprint (which was not certified by peer review) is the author/funder. All rights reserved. No reuse allowed without permission.

of spinning for human sperm, regardless of viscosity and capacitating conditions. The ability of human sperm to fertilize may be intimately related with head spinning, as capacitating medium were observed to excite a larger proportion of the population to spin. At last, the proposed methods can be applied to other free spinning objects and microorganisms that possess similar axis-symmetric body architecture to human spermatozoa.

Materials and Methods

Ethical approval for the human semen samples

The bioethics committee of the Institute of Biotechnology, UNAM approved the proposed protocols for the handling of human semen samples. Donors were properly informed regarding the experiments to be performed and each donor signed and agreed to a consent form. All samples fulfilled World Health Organization requirements for normal fertile semen samples.

Media

HTF (human tubal fluid) medium was used in this study. Non-capacitating HTF (pH 7.4) contained (mM): 4.7 KCl, 0.3 KH_2PO_4, 90.7 NaCl, 1.2 $MgSO_4$, 2.8 Glucose, 1.6 $CaCl_2$, 3.4 sodium pyruvate, 60 sodium lactate and 23.8 HEPES. Capacitating medium (pH 7.4) was HTF medium supplemented with 5 mg/ml BSA and 2 mg/ml $NaHCO_3$. Capacitating recording medium (pH 7.4) was only supplemented with 2 mg/ml $NaHCO_3$, BSA was not added. For viscous medium, 1% methyl cellulose was added to the non-capacitating or capacitating recording medium, depending on the experimental condition.

Biological preparations

bioRxiv preprint doi: https://doi.org/10.1101/2022.11.28.517870; this version posted November 29, 2022. The copyright holder for this preprint (which was not certified by peer review) is the author/funder. All rights reserved. No reuse allowed without permission.

Semen samples were obtained by masturbation from healthy donors after 48 h of sexual abstinence. Highly motile sperm were recovered after the swim-up protocol. Briefly, 300 µl of semen were placed in a test tube, then 1 ml of non-capacitating or capacitating medium, depending on the experimental condition, was added on top. Tubes were incubated at a 45º angle, at 37ºC in a humidified atmosphere of 5% CO_2 and 95% air during 1 h. Then, sperm from the medium on top were collected and concentration was adjusted to 10^6 cells/ml. To promote *in vitro* capacitation, sperm in capacitating medium were incubated for an additional 5 h. Recordings were performed in (a) non-capacitating aqueous and viscous medium, and (b) capacitating aqueous or viscous medium.

Sperm samples

A total of 409 freely swimming spermatozoa (30 samples -one per day- from 9 different donors) were analyzed: (a) 180 non-capacitated (78 in aqueous media and 102 in viscous media) and (b) 229 in capacitating media (106 in aqueous media and 123 in viscous media).

3D Imaging Microscopy

Multifocal plane stacks were acquired with the system originally described in Corkidi et al., 2008, consisting on an inverted Olympus IX71 microscope, mounted on an optical table [TMC (GMP SA, Switzerland)], reconfigured with a piezoelectric device P-725 (Physik Instrumente, MA, USA) which periodically displaces a high magnification 100x objective (Olympus UPlanSApo 100x/1.4 na oil objective) at a frequency of 80Hz with a z displacement of 20 μm. A high-speed camera NAC Q1v (Nac Americas, Inc., USA) acquired images at a rate of 8000 fps with 640 x 480 pixels resolution. Every rising movement of the piezo device (half cycle i.e., 1/160 sec) contains 50 different focal planes

bioRxiv preprint doi: https://doi.org/10.1101/2022.11.28.517870; this version posted November 29, 2022. The copyright holder for this preprint (which was not certified by peer review) is the author/funder. All rights reserved. No reuse allowed without permission.

(1 image per focal plane). The high-speed camera can store 28,000 images (RAM is 8 Gb) per cell, thus recording spinning motion for a total of 3.5 seconds. Since in this work the rotation of the sperm head is a critical aspect, every possible inversion in each single element conforming the optical-electronical pipeline's path had to be carefully considered (inverted microscope, camera driver setup, image processing software and for visualization -Fiji, Matlab, Paraview, etc.-). As a control test, we have placed in the microscope stage (using a 4x objective) a known pattern (a character R in a piece of paper) viewing the front face of the objective (upside down if seen by the top of the microscope). We have verified that the character appeared upright in the computer screen and that it moved accordingly with the horizontal and vertical stage movements (seen the stage from the bottom-top direction where the objective is placed).

Acknowledgements

The authors thank Paulina Torres for helpful assistance with experimental procedures and Shirley Ainsworth for bibliographic support. The help of Juan Manuel Hurtado, Roberto Rodríguez, Omar Arriaga and Arturo Ocádiz regarding computer services is acknowledged.

Competing interests

The authors declare that no competing interests exit.

Funding

bioRxiv preprint doi: https://doi.org/10.1101/2022.11.28.517870; this version posted November 29, 2022. The copyright holder for this preprint (which was not certified by peer review) is the author/funder. All rights reserved. No reuse allowed without permission.

691 The following grantig institutions are acknowledged for their support: Consejo Nacional de
692 Ciencia y Tecnología (CONACyT-Mexico), grants 255914 and Fronteras; Dirección
693 General de Asuntos del Personal Académico/ Universidad Nacional Autónoma de México
694 (DGAPA/ UNAM), grants: IN200919 to AD; IN105222 to GC. PH acknowledges support
695 from Chan Zuckerberg Initiative DAF Grant (2020-225643) and HG from DTP Engineering
696 and Physical Sciences Research Council.

697 **Author contributions**

698 Conception and design: G.C., F.M., H.G., A.D.; Acquisition of data: G.C., F.M., A-L.G.-C.,
699 Methodology: G.C., F.M., P.H.-H., A-L.G.-C, B.N.C., H.G., A.D.; Software: G.C., F.M.,
700 P.H.-H., B.N.C.; Resources: G.C., A.D.; Writing - review & editing: G.C., F.M., B.N.C.,
701 H.G., A.D.; Supervision, funding and project administration: G.C., A.D.

702 **Ethics**

703 The bioethics committee of the Institute of Biotechnology, UNAM approved the proposed
704 protocols for the handling of human semen samples. Donors were properly informed
705 regarding the experiments to be performed and each donor signed and agreed to a
706 consent form. All samples fulfilled World Health Organization requirements for normal
707 fertile semen samples.

708

bioRxiv preprint doi: https://doi.org/10.1101/2022.11.28.517870; this version posted November 29, 2022. The copyright holder for this preprint (which was not certified by peer review) is the author/funder. All rights reserved. No reuse allowed without permission.

709

References

Bishop DW. 1958. Motility of the Sperm Flagellum. Nature 182:1638-1640. https://doi.org/10.1038/1821638a0

Blokhuis EWM. 1961. Optical Investigations on the Movement of Bull Spermatozoa. In: Proceedings of 4th International Congress on Animal Reproduction, The Hague 2:243-248.

Bukatin A, Kukhtevich I, Stoop N, Dunkel J, Kantsler V. 2015. Bimodal rheotactic behavior reflects flagellar beat asymmetry in human sperm cells. PNAS 112:15904–15909. https://doi.org/10.1073/pnas.1515159112

Bukatin A, Kukhtevich I, Stoop N, Dunkel J, Kantsler V. 2016. Bimodal rheotactic behavior reflects flagellar beat asymmetry in human sperm cells. PNAS 112:15904–15909. https://doi.org/10.1073/pnas.1515159112

Camelet S, Jülicher F. 2000. Generic aspects of axonemal beating. New Journal of Physics 2:24.1-24.3. https://www.pks.mpg.de/fileadmin/user_upload/MPIPKS/group_pages/BiologicalPhysics/juelicher/publications/2000-2003/nj0124.pdf

Corkidi G, Hernández-H P, Montoya F, Gadêlha H, Darszon A. 2021. Long-term segmentation-free assessment of head–flagellum movement and intracellular calcium in swimming human sperm. Journal of Cell Science 134:jcs250654. https://doi.org/10.1242/jcs.250654

Corkidi G, Taboada B, Wood CD, Guerrero A, Darszon A. 2008. Tracking Sperm in Three Dimensions. Biochemical and Biophysical Research Communications 373:125–129. https://doi.org/10.1016/j.bbrc.2008.05.189

Daloglu MU, Luo W, Shabbir F, Lin F, Kim K, Lee I, Jiang JQ, et al.. 2018. Label-Free 3D Computational Imaging of Spermatozoon Locomotion, Head Spin and Flagellum Beating over a Large Volume. Light: Science & Applications 7:17121–17121. https://doi.org/10.1038/lsa.2017.121

Dardikman YG, Mirsky S, Barnea I, Shaked NT. 2020. High-resolution 4-D acquisition of freely swimming human sperm cells without staining. Science Advances 6:eaay7619. https://doi.org/10.1126/sciadv.aay7619

David G, Serres C, Jouannet P. 1981. Kinematics of Human Spermatozoa. Gamete Research 4:83-95. https://doi.org/10.1002/mrd.1120040202

Denehy MA, Herbison-evans D, Denehy BV. 1975. Rotational and Oscillatory Components of the Tailwave in Ram Spermatozoa. Biology of Reproduction 13:289-297. https://doi.org/10.1093/biolreprod/13.3.289

Drake AD. 1974. Observations on bull sperm rotation. Biology of Reproduction 10:78-84. https://doi.org/10.1095/biolreprod10.1.78

Fawcett DW. 1975. The Mammalian Spermatozoon. Developmental Biology 44:394–436. https://doi.org/10.1016/0012-1606(75)90411-X

Gadêlha H, Gaffney EA, Smith DJ, Kirkman-Brown JC. 2010. Nonlinear instability in flagellardynamics: A novel modulation mechanism in sperm migration?. Journal of The Royal Society Interface 7:1689-1697. 10.1098/rsif.2010.0136

Gadêlha H, Gaffney EA. 2019. Flagellar ultrastructure suppresses buckling instabilities and enablesmammalian sperm navigation in high-viscosity media. Journal of The Royal Society Interface 16:20180668. https://doi.org/10.1098/rsif.2018.0668

Gadêlha H, Hernández-Herrera P, Montoya F, Darszon A, Corkidi G. 2020. The human sperm beats anisotropically and asymmetrically in 3D. Science Advances sciadv.aba5168:. https://doi.org/10.1126/sciadv.aba5168

Gaffney EA, Gadêlha H, Smith DJ, Blake JR, Kirkman-Brown JC. 2011. Mammalian sperm

bioRxiv preprint doi: https://doi.org/10.1101/2022.11.28.517870; this version posted November 29, 2022. The copyright holder for this preprint (which was not certified by peer review) is the author/funder. All rights reserved. No reuse allowed without permission.

motility: Observation and theory. Annual Review of Fluid Mechanics 43:501-528. https://www.annualreviews.org/doi/abs/10.1146/annurev-fluid-121108-145442
Goodman J. 2005. Introduction to Fourier optics. McGraw-Hill 3rd ed:.
Hernandez HO, Hernandez-H P, Montoya F, Olveres J, Bloomfield-G H, Darszon A, Escalante-R B, Corkidi G. 3D+t feature-based descriptor for unsupervised flagellar human sperm beat classification 2022488-492doi:10.1109/EMBC48229.2022.9871419
Ishijima S, Hamaguchi MS, Naruse M, Ishijima SA, Hamaguchi Y. 1992. Rotational movement of a spermatozoon around its long axis. Journal of Experimental Biology 163:15–31.
Ishimoto K, Gadêlha H, Gaffney EA, Smith DJ, Kirkman-Brown J. 2017. Coarse-graining the fluid flow around a human sperm. Physical Review Letters 118:124501. https://doi.org/10.1103/PhysRevLett.118.124501
Keller HE, Spring KR, Flynn BO, Davidson MW. 2022. Focus depth and spherical aberration. Olympus Microscopy Resource Centre :. https://www.olympus-lifescience.com/en/microscope-resource/primer/java/aberrations/pointspreadaberration/
Kidger MJ. 2002. Fundamental Optical Design. :.
Lee S-H, Grier DG. 2007. Holographic microscopy of holographically trapped three_dimensional structures. Optics Express 15:1505-1512. https://DOI: 10.3109/01485017908987307
Leung MR, Roelofs MC, Ravi RT, Maitan P, Henning H, Zhang M, Bromfield EG, et al.. 2021. The Multi-Scale Architecture of Mammalian Sperm Flagella and Implications for Ciliary Motility. The EMBO Journal 40:e107410. https://doi.org/10.15252/embj.2020107410
Linnet L. 1979. Human Spermatozoa: Unidirectional Rotation of the Tail as Indicated by Head-to-Head Agglutinates. Archives of Andrology 2:157-161. https://10.3109/01485017908987307
Liu CH, Tzeng OJL, Hung DL, Tseng P, Juan CH. 2012. Investigation of bistable perception with the ‘‘silhouette spinner’’: Sit still, spin the dancer with your will. Vision Research 60:34-39. https://doi.org/10.1016/j.visres.2012.03.005
Miller MR, Kenny SJ, Mannowetz N, Mansell SA, Wojcik M, Mendoza S, Zucker RS, Xu K, Lishko PV. 2018. Asymmetrically Positioned Flagellar Control Units Regulate Human Sperm Rotation. Cell Reports 24:2606–2613. https://doi.org/10.1016/j.celrep.2018.08.016
Muschol M, Wenders C, Wennemuth G. 2018. Four-dimensional analysis by high-speed holographic imaging reveals a chiral memory of sperm flagella. PLoS ONE 13:e0199678. https://doi.org/10.1371/journal.pone.0199678
Oriola D, Gadêlha H, Casademunt J. 2017. Nonlinear amplitude dynamics in flagellar beating. Royal Society Open Science 4:160698. https://royalsocietypublishing.org/doi/pdf/10.1098/rsos.160698
Phillips DM Direction of Rolling in Mammalian Spermatozoa 1983. André, J. (eds) Springer, Dordrecht . https://doi.org/10.1007/978-94-009-7675-7_63
Phillips DM Direction of Rolling of Squirrel Spermatozoa 1997. In: Motta, PM 2nd International Malpighi Symposium 47-50.
Phillips DM. 1972. Comparative Analysis of Mammalian Sperm Motility. The Journal of Cell Biology 53:561-573. https://doi.org/10.1083/jcb.53.2.561
Pimentel JA, Carneiro J, Darszon A, Corkidi G. 2012. A segmentation algorithm for automated tracking of fast swimming unlabelled cells in three dimensions. Journal of Microscopy 245:72-81. 10.1111/j.1365-2818.2011.03545.x
Powar S, Yazdan PF, Nandagiri A, Gaikwad AS, Potter DL, O’Bryan MK, Prabhakar R, Soria J, Nosrati R. 2022. Unraveling the Kinematics of Sperm Motion by Reconstructing the Flagellar Wave Motion in 3D. Small Methods 6:2101089. https://doi.org/10.1002/smtd.202101089
Riedel-Kruse IH, Hilfinger A, Howard J, Jülicher F. 2007. How molecular motors shape the flagellarbeat. HFSP Journal 1:192-208. https://doi.org/10.2976/1.2773861
Rikmenspoel R. 1965. The Tail Movement of Bull Spermatozoa: Observations and Model Calculations. Biophysical Journal 5:365-392. https://doi.org/10.1016/S0006-3495(65)86723-6

bioRxiv preprint doi: https://doi.org/10.1101/2022.11.28.517870; this version posted November 29, 2022. The copyright holder for this preprint (which was not certified by peer review) is the author/funder. All rights reserved. No reuse allowed without permission.

Sartori P, Geyer VF, Scholich A, Jülicher F, Howard J. . Dynamic curvature regulation accounts for the symmetric and asymmetric beats of Chlamydomonas flagella. eLife 5:e13258. https://doi.org/10.7554/eLife.13258
Schindelin J, Arganda-C I, Frise E, Kaynig V, Longair M, Pietzsch T, … Cardona A. 2012. Fiji: an open-source platform for biological-image analysis. Nature Methods 9:676-682. doi:10.1038/nmeth.2019
Silva-Villalobos F, Pimentel A, Darszon A, Corkidi G. 2014. Imaging of the 3D dynamics of flagellar beating in human sperm. Engineering in Medicine and Biology Society (EMBC), 2014 36th Annual International Conference of the IEEE :190 - 193. DOI: 10.1109/EMBC.2014.6943561
Smith D, Gaffney E, Blake J, Kirkman-Brown J. 2009. Human sperm accumulation near surfaces: A simulation study. Journal of Fluid Mechanics 621:289-320. https://doi.org/10.1017/S0022112008004953
Smith DJ, Gaffney EA, Gadêlha H, Kapur N, Kirkman-Brown JC. 2009. Bend Propagation in the Flagella of Migrating Human Sperm, and Its Modulation by Viscosity. Cell Motility and the Cytoskeleton 66:220-236. https://doi.org/10.1002/cm.20345
Suarez SS. 2016. Mammalian sperm interactions with the female reproductive tract . Cell and Tissue Research 363:185-194. https://doi.org/10.1007/s00441-015-2244-2
Wilson L, Zhang R. 2012. 3D localization of weak scatterers in digital holographic microscopy using Rayleigh-Sommerfeld back-propagation. Optics Express 20:16735–16744.
Woolley DM Interpretations of the pattern of sperm tail movements 1979. ed. D. W. Fawcett and J. M. Bedford Baltimore-Munich: Urban& Schwarzenberg 69-79.
Woolley DM, Osborn IW. 1984. Three-Dimensional Geometry of Motile Hamster Spermatozoa. Journal of Cell Science 67:159-170. https://doi.org/10.1242/jcs.67.1.159
Woolley DM. 1977. Evidence for 'Twisted Plane' Undulations in Golden Hamster Sperm Tails. The Journal of Cell Biology 75:851-865. https://doi.org/10.1083/jcb.75.3.851
Yanhe Z, Wang H, Wiesehoefer C, Shah NB, Reetz E, Hwang JY, Huang X, et al.. 2022. 3D Structure and in Situ Arrangements of CatSper Channel in the Sperm Flagellum. Nature Communications 13:3439. https://doi.org/10.1038/s41467-022-31050-8
Yeung, CH, Woolley DM. 1984. Three-dimensional bend propagation in hamster sperm models and the direction of roll in free-swimming cells. Cell Motil. 4:215-226. https://doi.org/10.1002/cm.970040306
Zaferani M, Javi F, Mokhtare A, Li P, Abbaspourrad A. 2021. Rolling controls sperm navigation in response to the dynamic rheological properties of the environment. eLife 10:e68693. https://doi.org/10.7554/eLife.68693

Supporting Information

Invariance of the method to sperm orientation

To investigate whether the direction of sperm rotation is not an artifact of the illumination setup of the microscope i.e., that the bright border of the sperm head edge is not an effect of the illumination setup, we analyzed the rotation of non-capacitated sperm swimming in four different directions in a Cartesian plane. As we explained previously, in the sequence

bioRxiv preprint doi: https://doi.org/10.1101/2022.11.28.517870; this version posted November 29, 2022. The copyright holder for this preprint (which was not certified by peer review) is the author/funder. All rights reserved. No reuse allowed without permission.

719 shown in Figure 6, it is clearly seen that the border of the narrowest part of the head is
720 naturally marked with a bright composed semi-circle. This bright feature turns in the
721 direction of the sperm head (note that this bright border is located behind the sperm head,
722 as explained before). We have verified that independently of the swimming trajectory of
723 sperm, the evolution on time of this bright semi-circle clearly defines the rotating direction
724 of the sperm head. Supplementary Figure S1 shows two consecutive time-points of 4
725 different sperm with outgoing trajectories from the center of each of four Cartesian planes.
726 As can be seen in this figure, the bright region (due to the optical spherical aberration
727 contrast inversion effect) in each sperm always appears first on the ***b*** side of the head and
728 then it moves to the opposite ***b'*** side at the subsequent time-point (see Figure 9). This
729 indicates that all the sperm rotate in a CCW (since the bright border is behind the head of
730 the sperm) direction independently of the direction of the sperm trajectory (four quadrants).

bioRxiv preprint doi: https://doi.org/10.1101/2022.11.28.517870; this version posted November 29, 2022. The copyright holder for this preprint (which was not certified by peer review) is the author/funder. All rights reserved. No reuse allowed without permission.

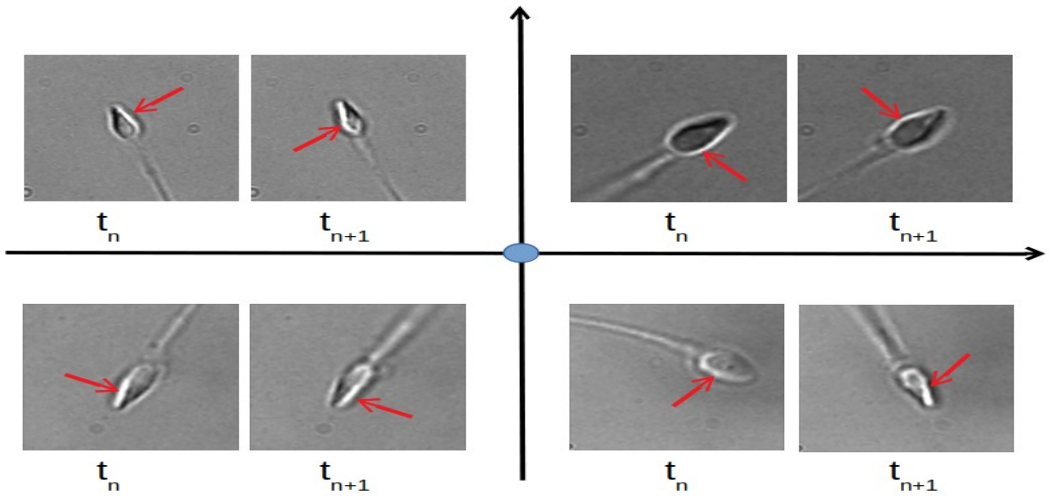

Figure S1. Four different non-capacitated sperm with outgoing trajectories from the center of each of the four Cartesian planes (blue circle). Two different time-points (t_n and t_{n+1}) are shown for each sperm. The bright region (due to the optical spherical aberration contrast inversion effect) always appears first in the left side of the head and then moves to the right side at the subsequent time-point (from head to tail) indicating a CCW head spinning as shown in Results. The red arrows indicate the bright border in each image.